

Defect turbulence in a dense suspension of polar, active swimmers

Navdeep Rana

Max Planck Institute for Dynamics and Self-Organization (MPIDS), D-37077 Göttingen, Germany

Rayan Chatterjee

Stanford Medicine, Stanford University, USA

Sunghan Ro and Dov Levine

Department of Physics, Technion-Israel Institute of Technology, Haifa 3200003, Israel

Sriram Ramaswamy

Department of Physics, Indian Institute of Science, Bengaluru 560 012 India

Prasad Perlekar*

Tata Institute of Fundamental Research, Hyderabad, India

We study the effects of inertia in dense suspensions of polar swimmers. The hydrodynamic velocity field and the polar order parameter field describe the dynamics of the suspension. We show that a dimensionless parameter R (ratio of the swimmer self-advection speed to the active stress invasion speed [1]) controls the stability of an ordered swimmer suspension. For R smaller than a threshold R_1 , perturbations grow at a rate proportional to their wave number q . Beyond R_1 , we show that the growth rate is $\mathcal{O}(q^2)$ until a second threshold $R = R_2$ is reached. The suspension is stable for $R > R_2$. We perform direct numerical simulations to investigate the steady state properties and observe defect turbulence for $R < R_2$. An investigation of the spatial organisation of defects unravels a hidden transition: for small $R \approx 0$ defects are uniformly distributed and cluster as $R \rightarrow R_1$. Beyond R_1 , clustering saturates and defects are arranged in nearly string-like structures.

I. INTRODUCTION

The instability [1, 2] of a viscous suspension of motile organisms leads to an abundance of ordered and chaotic states [3–10], of which *active turbulence* [11] has attracted much attention. The majority of studies have investigated this iconic phenomenon in *nematic* systems, in which the local structure and characteristic defects are associated with uniaxial fore-aft symmetric order. In a recent work [1], we established the stabilizing role of fluid inertia in the transition to active turbulence in *polar* active suspensions, in which the local order is vectorial. We discovered that the steady-state behavior of the suspension changed across two thresholds R_1 and R_2 in the dimensionless ratio $R \equiv \rho v_0^2 / \sigma$ of inertia and activity, where ρ is the mass density of the suspension, v_0 is the self-propulsion speed, and σ the mean active stress. We found defect turbulence for $R < R_1$, a fluctuating but ordered phase-turbulent steady state for $R_1 < R < R_2$, and a quiescent ordered state for $R > R_2$. The analysis of [1] considered only the suspension velocity and polar order-parameter fields \mathbf{u} and \mathbf{p} , implicitly treating the concentration of active particles as “fast”, as would happen, for example, if birth and death led to a nonzero relaxation rate at zero wavenumber.

Highly concentrated systems present another scenario where we can ignore fluctuations in the number den-

sity of suspended particles, albeit in a radically different manner. In such a limit, it is reasonable to make the approximation that concentration fluctuations are prohibited, which means that the solute velocity field or, equivalently, the polar order parameter \mathbf{p} , is solenoidal: $\nabla \cdot \mathbf{p} = 0$. We will term such systems as simply “dense”. See [12] for the implementation of such a condition in dry active matter.

In this paper, we study stability and turbulence in a dense suspension of polar active particles (DSPAP). Section II describes the equations of motion and in Section III, we conduct a linear stability analysis of an ordered suspension with respect to perturbations with wavenumber q . We show that for extensile suspensions, the same dimensionless parameter R as in [1] governs the linear stability of the suspension. For $R < R_1 \equiv 1 + \lambda$, where λ is the flow-alignment parameter, we find an inviscid instability where the most unstable pure bend modes grow at a rate $\propto q$. For $R_1 < R < R_2$, we find that the pure bend perturbations grow at a rate $\propto q^2$. Finally for $R > R_2$, orientational order is linearly stable. These instability mechanisms are identical to those in our earlier report [1]. Further, dense suspensions of *contractile* swimmers are linearly stable. Next, in Section IV, we study the steady-state properties of the suspension using numerical simulations. We show the presence of vortex-defect turbulence for $R < R_2$. Correlation length grows as we increase R and appears to diverge at $R \approx R_2$. Interestingly we do not observe a phase-turbulent regime [1]. Instead, a detailed analysis of the spatial organization of defects using correlation dimension d_2 reveals a

* perlekar@tifrh.res.in

novel morphological transition. We find that defects are uniformly distributed ($d_2 \approx 2$) for $R \rightarrow 0$ (Stokesian suspension) and start to cluster on increasing R . Maximum clustering ($d_2 \approx 1$) is attained around $R = R_1$, and we observe that defects organize into stringy patterns. No further changes in defect organization are observed on increasing R beyond R_1 .

II. EQUATIONS OF MOTION

We use a hydrodynamic formulation to study the dense suspension of polar active particles (DSPAP). In the incompressible limit (uniform suspension density and active particle concentration), the dynamics of the hydrodynamic velocity field $\mathbf{u}(\mathbf{x}, t)$ and the orientation order parameter $\mathbf{p}(\mathbf{x}, t)$ is described by the following equations [1–3, 13–15]:

$$\begin{aligned} \rho(\partial_t \mathbf{u} + \mathbf{u} \cdot \nabla \mathbf{u}) &= -\nabla P + \mu \nabla^2 \mathbf{u} + \nabla \cdot (\boldsymbol{\Sigma}^a + \boldsymbol{\Sigma}^r), \\ \partial_t \mathbf{p} + (\mathbf{u} + v_0 \mathbf{p}) \cdot \nabla \mathbf{p} &= -\nabla \Pi + (\lambda \mathbf{S} + \boldsymbol{\Omega}) \cdot \mathbf{p} + \Gamma \mathbf{h}, \\ \nabla \cdot \mathbf{u} &= 0, \text{ and } \nabla \cdot \mathbf{p} = 0. \end{aligned} \quad (1)$$

Here, ρ is the suspension density, μ is the fluid viscosity, v_0 is the self-advection speed of the swimmers, λ is the flow alignment parameter, P is the hydrodynamic pressure that enforces incompressibility of the velocity field, Π is the pressure-like term that enforces incompressibility of the order parameter field \mathbf{p} imposed by the constant concentration approximation, $\mathbf{S} \equiv (\nabla \mathbf{u} + \nabla \mathbf{u}^T)/2$ and $\boldsymbol{\Omega} \equiv (\nabla \mathbf{u} - \nabla \mathbf{u}^T)/2$ are the symmetric and anti-symmetric parts of the velocity gradient tensor $\nabla \mathbf{u}$. $\boldsymbol{\Sigma}^a \equiv -\sigma_0 \mathbf{p} \mathbf{p}$ is the leading order apolar intrinsic stress associated with the swimming activity where the force-dipole density $\sigma_0 > 0 (< 0)$ for extensile (contractile) swimmers [2], $\boldsymbol{\Sigma}^r \equiv -\lambda_+ \mathbf{h} \mathbf{p} - \lambda_- \mathbf{p} \mathbf{h}$ is the reversible thermodynamic stress [15] with $\lambda_{\pm} = (\lambda \pm 1)/2$, $\mathbf{h} = -\delta F / \delta \mathbf{p}$ is the molecular field conjugate to \mathbf{p} with the free-energy functional

$$F = \int d^d r \left[\frac{K}{2} |\nabla \mathbf{p}|^2 + \frac{1}{4} (\mathbf{p} \cdot \mathbf{p} - 1)^2 \right],$$

that favors an aligned order parameter state with unit magnitude, and Γ is the rotational mobility for the relaxation of the order parameter field to the uniform ordered state prescribed by the free energy dynamics. For simplicity, we choose a single Frank constant K , which penalizes the gradients in \mathbf{p} [16]. We are primarily interested in the interplay of the self-propulsion speed v_0 and the leading order apolar active stress, hence similar to our earlier study [1], we have ignored the contribution from higher-order polar gradient terms in $\boldsymbol{\Sigma}^a$.

III. LINEAR STABILITY ANALYSIS

We analyse the stability of the ordered state $(\mathbf{u}, \mathbf{p}) = (0, \hat{\mathbf{x}})$ to small monochromatic perturbations of the form

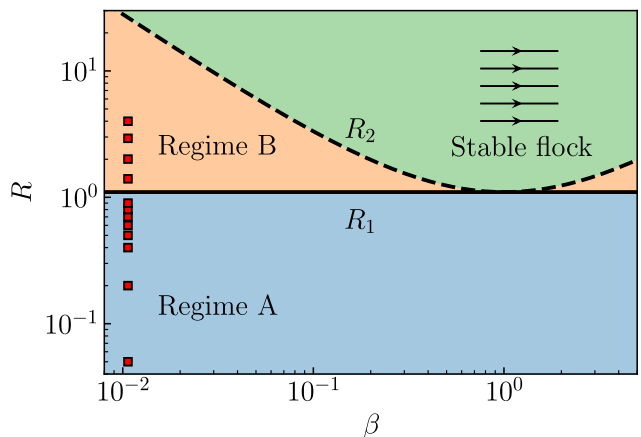


FIG. 1. $R - \beta$ phase diagram highlighting different stability regimes for incompressible polar active suspensions. In both the unstable regimes A and B, we observe defect turbulence (see Section IV). Red squares mark the simulations on the $R - \beta$ plane with $\beta = 10^{-2}$, $R_1 = 1.1$, and $R_2 = 28$. See Table I for the rest of parameters.

$(\delta \mathbf{u}, \delta \mathbf{p}) = (\hat{\mathbf{u}}, \hat{\mathbf{p}}) e^{i(\mathbf{q} \cdot \mathbf{x} - \omega t)}$, where \mathbf{q} is the perturbation wavevector and ω is the frequency. As dense contractile suspension are linearly stable, here, we focus our study on extensile suspension. In what follows, we discuss the results for pure-bend perturbations, the most unstable modes for extensile systems [1, 4]. For a detailed discussion of the linear stability analysis including the stability of twist-bend and splay-bend modes, we refer the reader to Appendix A. A large wavelength (small q) expansion up to $\mathcal{O}(q^2)$ yields the following dispersion relation for the pure-bend modes:

$$\begin{aligned} 2\omega_{\pm} &= v_0 \left(1 \pm \sqrt{1 - R_1/R} \right) q \\ &+ i \frac{\mu}{\rho} \left(\pm \frac{(1 - \beta)}{\sqrt{1 - R_1/R}} - (1 + \beta) \right) q^2, \end{aligned} \quad (2)$$

where we have defined the dimensionless numbers $R \equiv \rho v_0^2 / 2\sigma_0$, $R_1 \equiv 1 + \lambda$ and $\beta = \Gamma K \rho / \mu$. In Fig. 1, we show a qualitative phase diagram highlighting the three different stability regimes. In regime A, $R < R_1$ and irrespective of the value of β , pure-bend modes are unstable with a growth rate $\Im(\omega) \propto q$. In regime B, $R_1 < R < R_2$ where $R_2 \equiv R_1 (1 + \beta)^2 / 4\beta$, pure-bend modes grow at a rate $\Im(\omega) \propto q^2$. Finally, in regime C, when $R > R_2$ the ordered state is stable.

IV. DIRECT NUMERICAL SIMULATIONS

We perform direct numerical simulations of (1) on a square domain of area L^2 discretized with N^2 equispaced collocation points. Similar to [1], we use a pseudo-spectral method for spatial integration of the velocity field and a fourth-order finite difference method

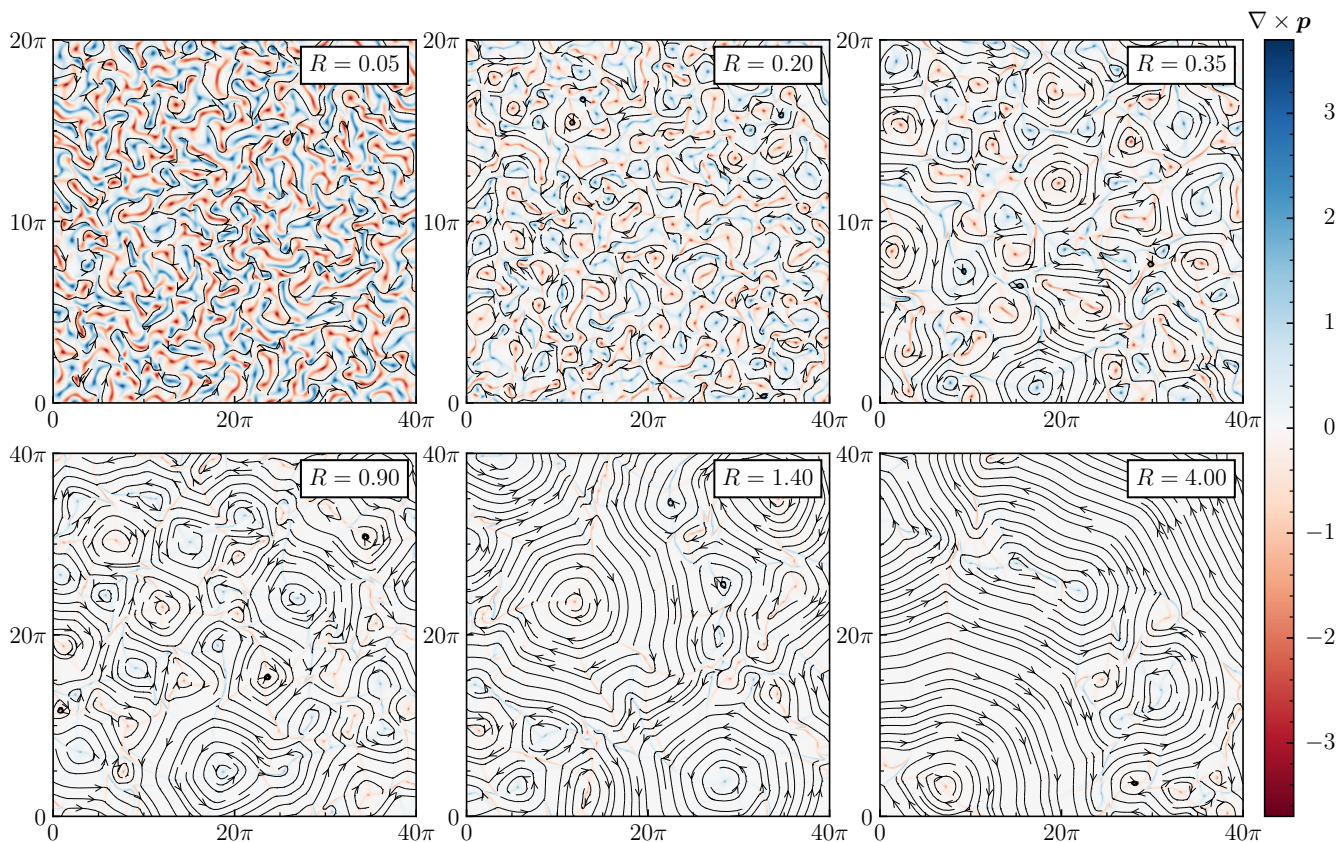


FIG. 2. Order parameter streamlines superimposed over pseudocolor plot of $\nabla \times \mathbf{p}$ highlighting vortices at different values of R . For $R \geq 0.9$, we only show a subdomain of size $(40\pi)^2$. Inter-defect separation grows with increasing R . For $R < R_1 = 1.1$, we find that the defects are uniformly distributed over the simulation domain, but form clusters for $R > R_1$ (See also Fig. 5).

for the order parameter. For time marching we use a second-order Adams-Bashforth scheme [17], and the incompressibility condition in the order-parameter field is implemented using an operator-splitting method [18]. We undertake high-resolution numerical studies at various values of R and fixed $\beta = 10^{-2}$ to characterize the turbulent states arising from the instabilities of the ordered state. We initialize our simulations with a perturbed ordered state $\mathbf{u}(\mathbf{x}, 0) = \mathbf{0} + A \sum_{i=1}^{10} \cos(q_i x) \hat{y}$ and $\mathbf{p}(\mathbf{x}, 0) = \hat{x} + B \sum_{i=1}^{10} \cos(q_i x) \hat{y}$, where $q_i = i(2\pi/L)$, and choose $A = B = 10^{-3}$. For $R < R_2$, the perturbations destabilise the flow and a defect turbulence state is achieved. Table I summarizes all our simulation parameters. In what follows, we discuss the statistical properties of defect turbulence with varying R .

A. Defect turbulence

In Fig. 2 we show the streamlines of the order parameter field \mathbf{p} in the statistically steady state at different values of R . In both regimes A and B, the order parameter field shows vortices and saddles, with no evidence of global polar order. Asters and spirals are ruled out by

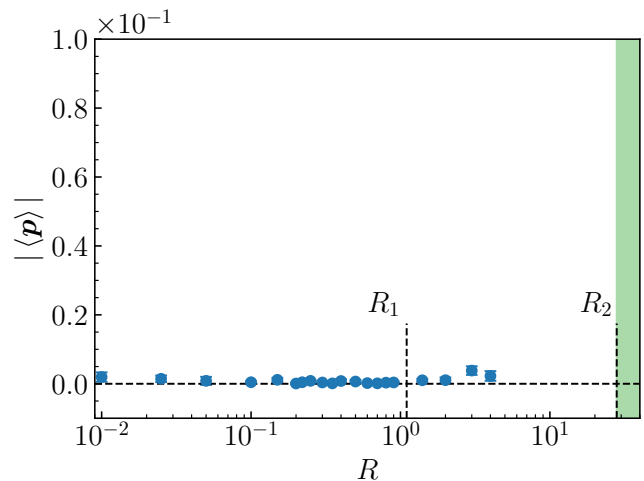


FIG. 3. Average order $|\langle \mathbf{p} \rangle|$ in the steady state at different R . For a disordered state $|\langle \mathbf{p} \rangle| = 0$ and for perfect alignment, $|\langle \mathbf{p} \rangle| = 1$. We do not observe any order in regime A or regime B. Ordered state is stable to perturbations in the green shaded region ($R > R_2$). The error bars are smaller than the markers.

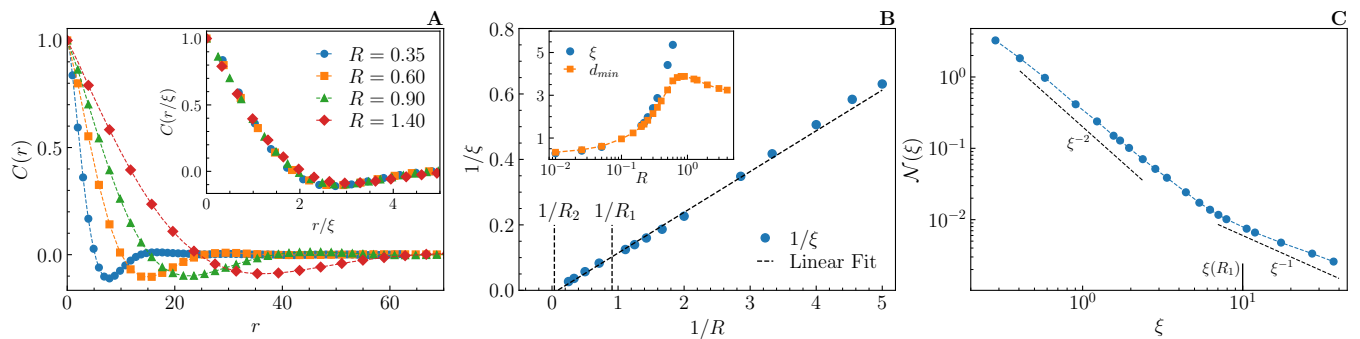


FIG. 4. (A) Steady state correlation function $C(r)$ for different values of R . (Inset) Correlation function collapse onto a single curve when distance is scaled by the correlation length ξ . (B) Plot of the inverse correlation length $1/\xi$ versus $1/R$. From the intercept of the linear fit on the $1/R$ axis, we conclude that ξ diverges around $R \approx R_2$. Inset: Comparison between the correlation length ξ and average nearest-neighbour distance d_{min} . For small R , ξ and d_{min} are identical. For large R , d_{min} saturates and ξ diverges. (C) Defect density $\mathcal{N}(\xi)$ as a function of the correlation length ξ . We observe two distinct scaling regimes for $R < R_1$ ($> R_1$). Vertical black line marks the correlation length $\xi(R = R_1)$ computed from the linear fit in (B).

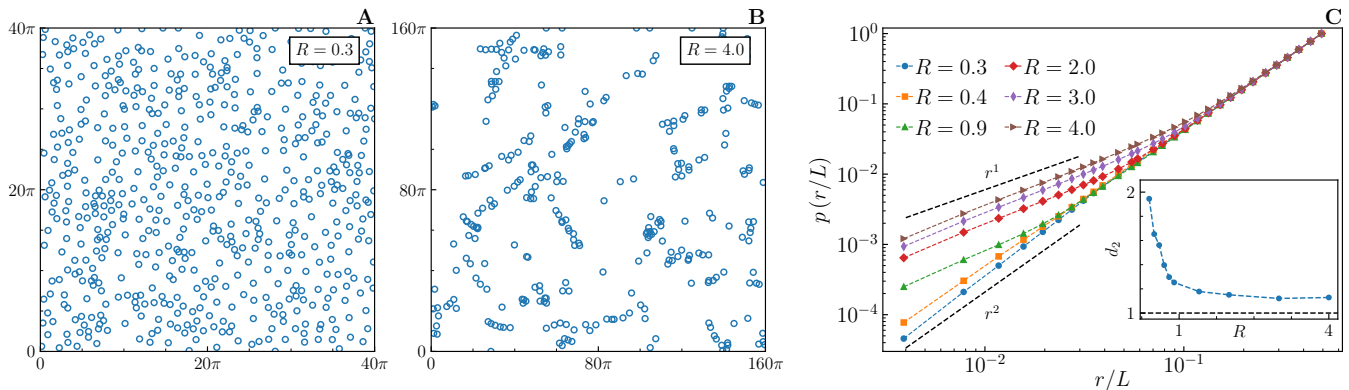


FIG. 5. (A,B) Scatter plot of the vortex cores for $R = 0.3$ and $R = 4.0$ respectively. For $R = 0.3$ and $R \ll R_1$ in general, defects are uniformly distributed over the simulation domain. For $R \gtrsim R_1$, we observe clustering of defects on one-dimensional string like structures. (C) Plot of the cumulative radial distribution function $p(r)$ for different values of R . At smaller distances, we observe $p(r) \sim r^{d_2}$, with $d_2 \sim 2$ for $R \ll R_1$ and $d_2 \sim 1$ for $R \geq R_1$. At distances larger than typical cluster size, $p(r) \sim r^2$ shows the same scaling for all R . Note that we have rescaled each $p(r)$ curve by its maximum value to highlight different scaling regimes. Inset: Variation of the correlation dimension d_2 vs R obtained from least-square fit on $p(r)$ for small r .

the incompressibility constraint. To further verify that the turbulent states lack global order, we compute the magnitude of the average polar order parameter $|\langle \mathbf{p} \rangle|$ in

L	N	$R \equiv \rho v_0^2 / 2\sigma_0$
10π	1024	0.05
40π	2048	0.2 – 0.4*
80π	4096	0.5
160π	4096	0.6 – 0.9†
160π	4096	1.4, 2, 3, 4

TABLE I. Parameters used in our simulations: $\rho = 1$, $\lambda = 0.1$, $\mu = 0.1$, $K = 10^{-3}$, $v_0 = 3.16 \times 10^{-2}$, and $\Gamma = 1$ are kept fixed for all runs. This sets $\beta = 10^{-2}$, $R_1 = 1.1$, and $R_2 = 28$. We vary R by varying σ_0 . Superscript * (†) indicate increments of 0.05 (0.1).

the statistical steady state at different values of R , where $\langle \dots \rangle$ denotes spatio-temporal averaging. Note that for the disordered states, $|\langle \mathbf{p} \rangle| = 0$, whereas $|\langle \mathbf{p} \rangle| = 1$ for a perfectly aligned state. In Fig. 3 we plot $|\langle \mathbf{p} \rangle|$ with increasing R , and, as expected, it is close to zero in both the unstable regimes.

B. Defect correlations and clustering

In Fig. 4(A), we plot the isotropic correlation function

$$C(r) = \frac{\langle \mathbf{p}(\mathbf{x} + \mathbf{r}) \cdot \mathbf{p}(\mathbf{x}) \rangle}{\langle \mathbf{p}(\mathbf{x}) \cdot \mathbf{p}(\mathbf{x}) \rangle}, \quad (3)$$

where $\langle \dots \rangle$ denote ensemble and angle averaging, for different values of R . With increasing R , the correlations of the order parameter increase. We fit the functional form

$C(r) = e^{-\left(\frac{r}{\xi}\right)^\delta}$ at small $r \ll L$ to extract the correlation length ξ and the exponent δ which decreases monotonically from $\delta \approx 1.7$ for $R = 0.2$ to $\delta \rightarrow 1$ for large R . The correlation function $C(r)$ collapses onto a unique curve when plotted versus the scaled separation r/ξ (see Fig. 4(A,inset)). In Fig. 4(B), we show that the correlation length ξ increases with R , and from the intercept of the linear fit on the $1/R$ axis, it appears to diverge at $R = R_2$. Note that investigating the spatial structure of the order parameter field for $R \rightarrow R_2$ becomes numerically unfeasible as $\xi \rightarrow \infty$ and finite-size effects become important.

To quantify the spatial distribution of the defect cores, we begin by identifying the defect coordinates. In Fig. 4(B,inset), we plot the average nearest-neighbor separation d_{min} for different values of R . For $R < R_1$, the correlation length ξ and d_{min} are indistinguishable, indicating that a unique length scale describes the defect dynamics [19]. In contrast, for $R > R_1$, correlation length increases, whereas the average nearest neighbour separation d_{min} saturates. Consequently, in Fig. 4(C), the defect number density $\mathcal{N}(\xi)$ (number of defects per unit area), also scales differently with the correlation length ξ for $R < R_1$ and $R > R_1$. For $R < R_1$, where a single length scale governs the dynamics, we observe $\mathcal{N}(\xi) \sim \xi^{-2}$, which indicates that the defects are distributed uniformly over the entire domain [20–22]. In contrast, for $R > R_1$, we find that $\mathcal{N}(\xi) \sim \xi^{-1}$, indicating clustering of defects.

Indeed, the scatter plots of the defect coordinates in Fig. 5(A,B) indicate uniformly distributed defects for $R < R_1$, whereas they appear clustered for $R > R_1$. We further quantify the clustering by evaluating the correlation dimension d_2 from the defect positions. The correlation dimension d_2 is evaluated from the $r \rightarrow 0$ scaling behaviour of the probability $p(r)$ of finding two defects within a distance r [23, 24]. For $R \ll 1$, we find $d_2 \sim 2$, and it decreases with increasing R until it saturates around $d_2 \sim 1$ for $R > R_1$ (see Fig. 5(C)). Thus we conclude that in dense suspensions, the cross-over in the $O(q)$ to $O(q^2)$ instability around $R = R_1$ is marked by an intriguing defect clustering transition.

In order to gain further insight on the defect clustering transition, we compute the Shannon entropy density of the polar order parameter H_p and the defect arrangement H_D using a two-dimensional extension of the pattern matching method from information theory [25–27]. To find H_p , we apply the pattern matching method on the discretized orientation field [28]. For the entropy density H_D , we apply the pattern matching algorithm on a boolean field which is set to one at the defect locations and zero everywhere else (See Fig. 5). In Fig. 6, we plot H_p and H_D versus R . As the defect position field contains less information in comparison to the order parameter field, H_D is smaller than H_p for all R . Both entropy densities decrease as we increase R , and scale inversely with the correlation length roughly as $H_D, H_p \approx \xi^{-1.4}$. However, we could not capture a pronounced change in

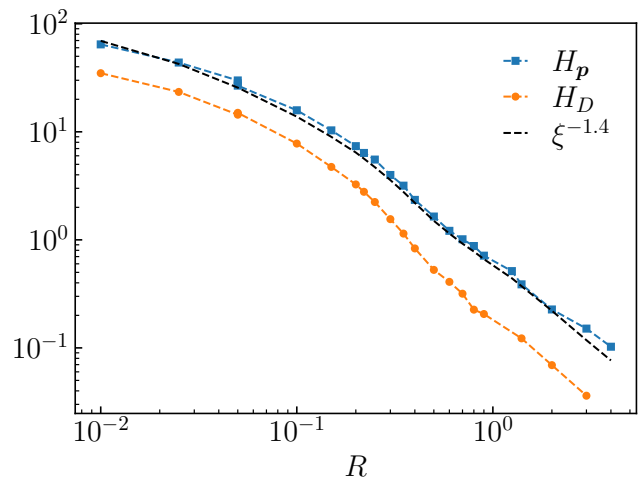


FIG. 6. Plot of the Shannon entropy density H_p of the polar order parameter and the Shannon entropy density of the defect arrangement H_D . With increasing R , both H_p and H_D decrease and scale roughly as $\xi^{-1.4}$ (dashed black guiding line).

the trend of H_p or H_D that corresponds to the clustering transition around $R \simeq R_1$.

C. Energy Spectrum

The shell-averaged energy spectra for the velocity and the order parameter field is defined as

$$\begin{aligned} E_u(q) &= \sum_{q-\frac{1}{2} \leq |\mathbf{m}| < q+\frac{1}{2}} |\hat{\mathbf{u}}_{\mathbf{m}}|^2, \text{ and} \\ E_p(q) &= \sum_{q-\frac{1}{2} \leq |\mathbf{m}| < q+\frac{1}{2}} |\hat{\mathbf{p}}_{\mathbf{m}}|^2, \end{aligned} \quad (4)$$

where $\hat{\mathbf{u}}_{\mathbf{m}}$ and $\hat{\mathbf{p}}_{\mathbf{m}}$ are the Fourier coefficients of the velocity \mathbf{u} and the order parameter \mathbf{p} fields. In Fig. 7, we plot $E_u(q\xi)$ and $E_p(q\xi)$ for different values of R . Consistent with our correlation function plots, we find that the spectra collapses onto single curve for $q < q_\sigma$, where $q_\sigma = 2\pi/\ell_\sigma$ with $\ell_\sigma \equiv \mu/\sqrt{\rho\sigma_0}$. Order parameter spectra shows two distinct power law scaling regimes:

$$E_p(q\xi) = \begin{cases} q^2 & \text{for } \frac{2\pi}{L} < q < \frac{2\pi}{\xi} \\ q^{-3} & \text{for } \frac{2\pi}{\xi} < q < \frac{2\pi}{\ell_\sigma}, \end{cases} \quad (5)$$

where $\ell_\sigma = \mu/\sqrt{\rho\sigma_0}$, and L determines the smallest wavenumber available in the simulation domain. The q^{-3} scaling is consistent with Porod's law prediction [29].

The kinetic energy spectrum $E_u(q\xi)$ is determined by the balance of the viscous and active stresses

$$\langle\langle |\hat{\mathbf{u}}_{\mathbf{q}}|^2 \rangle\rangle \approx -\frac{\sigma_0}{2\mu q^2} \langle\langle \hat{\mathbf{u}}_{\mathbf{q}}^* \cdot \hat{\mathbf{f}}_{\mathbf{q}} \rangle\rangle, \quad (6)$$

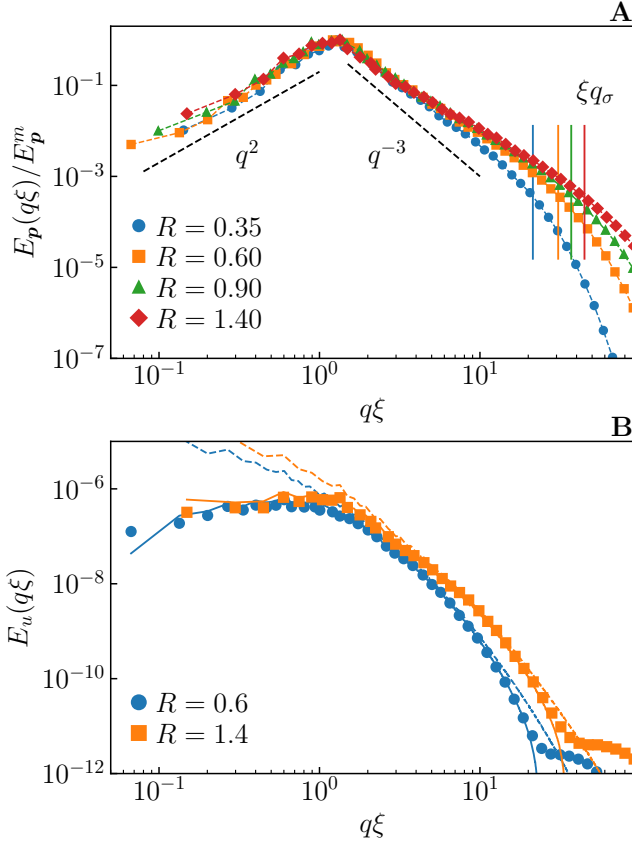


FIG. 7. (A) The order parameter energy spectrum $E_p(q\xi)$ for different values of R in both regime A and regime B. We scale the spectra by their respective peak values. $E_p(q\xi)$ shows a Porod scaling [29] for $1 < q\xi < q_\sigma \xi$. (B) Comparison of the kinetic energy spectrum $E_u(q\xi)$ (solid markers) with (6) (solid lines) and (7) (dashed lines) for two different values of R .

where $\hat{\mathbf{f}}_q = \mathcal{P} \cdot (i\mathbf{q} \cdot \hat{\mathbf{p}}\mathbf{p}_q)$, \mathcal{P} is the projection operator, and $\langle\langle \cdot \rangle\rangle$ denotes temporal averaging.

In Fig. 7 we show an excellent agreement between the energy spectrum obtained directly from the velocity field

and using (6), confirming the dominant balance between viscous and active stresses. Further assuming $\hat{\mathbf{f}}_q$ to be Gaussian random variables and using Gaussian integration by parts [30] we get

$$\langle\langle |\hat{\mathbf{u}}_q|^2 \rangle\rangle = \left\langle \left\langle \frac{\delta \hat{\mathbf{u}}_q}{\delta \hat{\mathbf{f}}_q} \right\rangle \right\rangle \langle\langle \hat{\mathbf{f}}_q^* \cdot \hat{\mathbf{f}}_q \rangle\rangle \approx \frac{\sigma_0^2}{2\mu^2 q^4} \langle\langle \hat{\mathbf{f}}_q^* \cdot \hat{\mathbf{f}}_q \rangle\rangle. \quad (7)$$

We observe that the prediction (7) matches well with the energy spectrum for $1 < q\xi < q_\sigma \xi$ (see Fig. 7).

V. CONCLUSIONS

We study spatio-temporal properties of dense wet suspensions of polar active particles. Using a linear stability analysis, we show how inertia can stabilize the orientational order against small perturbations. Our study reveals that the dimensionless parameter $R \equiv \rho v_0^2 / 2\sigma_0$ characterizes the stability of the aligned state. Although the neutral stability curve for DSPAP is identical to the previously studied case where concentration fluctuations are rendered fast [1], our numerical studies reveal that their steady-state properties are very different. For $R < R_2$ we observe defect turbulence, the order parameter flow consists of topological defects (vortices and saddles) with no global polar or nematic order. We unravel a hidden defect-ordering transition by investigating the spatial organization of defect centers. For $R = 0$, defects are uniformly distributed and start to cluster with increasing R . The clustering saturates around $R = R_1$ where we observe that the defects organize onto nearly one-dimensional string-like structures. Finally, we show that the spectrum of the order-parameter field shows a Porod's scaling for $q\xi \gg 1$ and a balance of viscous and apolar active stress determines the kinetic energy spectrum of the suspension velocity.

S. R. acknowledges research support from a J. C. Bose Fellowship of the SERB, India.

Appendix A: Linear stability analysis

We analyse the stability of the ordered state $\mathbf{u} = 0$, $\mathbf{p} = \hat{x}$ to small perturbations $\delta\mathbf{u} \equiv (\delta u_x, \delta\mathbf{u}_\perp)$ and $\delta\mathbf{p} \equiv (\delta p_x, \delta\mathbf{p}_\perp)$, where \perp denotes the plane perpendicular to the ordering. The linearised equations are

$$\begin{aligned} \rho \partial_t \delta u_x &= -\partial_x P + \mu \nabla^2 \delta u_x - \partial_x (\sigma_0 \delta p_x + \lambda_+ K \nabla^2 \delta p_x - 2\lambda \delta p_x), \\ \rho \partial_t \delta \mathbf{u}_\perp &= -\nabla_\perp P + \mu \nabla^2 \delta \mathbf{u}_\perp - \partial_x (\sigma_0 \delta \mathbf{p}_\perp + \lambda_+ K \nabla^2 \delta \mathbf{p}_\perp), \\ \partial_t \delta p_x &= -\partial_x \Pi - v_0 \partial_x \delta p_x + \Gamma K \nabla^2 \delta p_x - 2\Gamma \delta p_x + \lambda \partial_x \delta u_x, \\ \partial_t \delta \mathbf{p}_\perp &= -\nabla_\perp \Pi - v_0 \partial_x \delta \mathbf{p}_\perp + \Gamma K \nabla^2 \delta \mathbf{p}_\perp + \lambda_+ \partial_x \delta \mathbf{u}_\perp + \lambda_- \nabla_\perp \delta u_x. \end{aligned} \quad (A1)$$

Note that the perturbations also satisfy the incompressibility criteria, $\nabla \cdot \delta\mathbf{u} = 0$, and $\nabla \cdot \delta\mathbf{p} = 0$. To proceed further, we consider monochromatic perturbations of the form $(\delta\mathbf{u}, \delta\mathbf{p}) = (\hat{\mathbf{u}}, \hat{\mathbf{p}}) e^{i(\mathbf{q} \cdot \mathbf{x} - \omega t)}$, where $\mathbf{q} \equiv (q_x \hat{x} + \mathbf{q}_\perp \cdot \perp) = q(\cos \phi \hat{x} + \sin \phi \perp)$ is the perturbation wavevector and $\omega = \mathbb{R}(\omega) + i\mathbb{I}(\omega)$. Using incompressibility constraint we can

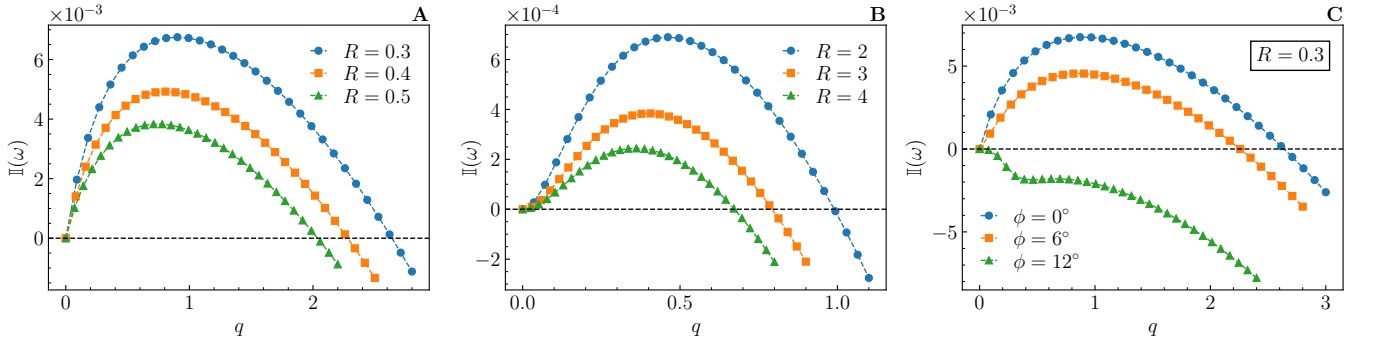


FIG. 8. (A, B) Growth rate $\mathbb{I}(\omega)$ vs. q for the most unstable pure bend modes at various R in regime A and B, respectively. With increasing R , the growth rate and the range of unstable wavenumbers decreases. (C) Growth rate $\mathbb{I}(\omega)$ vs. q for the splay-bend modes at small values of ϕ for a fixed $R = 0.3$.

eliminate pressure and longitudinal components to obtain

$$\begin{aligned} (-i\rho\omega + \mu q^2)\hat{\mathbf{u}}_{\perp} &= 2i\lambda q_x \frac{\mathbf{q}_{\perp} \cdot \hat{\mathbf{p}}_{\perp}}{q^2} \mathbf{q}_{\perp} - iq_x (\sigma_0 - \lambda_+ K q^2) \hat{\mathbf{p}}_{\perp} \\ (-i\omega + \Gamma K q^2 + iv_0 q_x)\hat{\mathbf{p}}_{\perp} &= -2\Gamma \frac{\mathbf{q}_{\perp} \cdot \hat{\mathbf{p}}_{\perp}}{q^2} \mathbf{q}_{\perp} + i\lambda_+ q_x \hat{\mathbf{u}}_{\perp}. \end{aligned} \quad (\text{A2})$$

The linear system (A2) is a set of four (two) coupled equations in three (two) dimensions and is easily solved by decomposing into splay-bend and twist-bend modes [1, 2, 31]. Taking a dot product with \mathbf{q}_{\perp} and solving for ω gives the following dispersion relation for the splay-bend modes

$$\begin{aligned} 2\omega_{\pm}^s &= v_0 q \cos \phi - i \frac{\mu_{\pm}}{\rho} q^2 - 2i\Gamma \sin^2 \phi \\ &\pm \frac{1}{\rho} \sqrt{(\rho v_0 q \cos \phi + i\mu_{\pm} q^2 - 2i\Gamma \sin^2 \phi)^2 - 4\rho\lambda_+ q^2 \cos^2 \phi (\sigma_0 - \lambda_+ K q^2 - 2\lambda \sin^2 \phi)}, \end{aligned} \quad (\text{A3})$$

where $\mu_{\pm} = \mu(1 \pm \beta)$. Similarly, a cross product with \mathbf{q}_{\perp} yields for the three dimensional twist-bend modes

$$2\omega_{\pm}^t = v_0 q \cos \phi - i \frac{\mu_{\pm}}{\rho} q^2 \pm \frac{1}{\rho} \sqrt{(\rho v_0 q \cos \phi + i\mu_{\pm} q^2)^2 - 4\rho\lambda_+ q^2 \cos^2 \phi (\sigma_0 - \lambda_+ K q^2)}. \quad (\text{A4})$$

In two dimensions ω just has two solutions given by (A3). Additionally, in a general description of polar suspensions, the concentration fluctuations only couples to the splay-bend modes, thus the dispersion relation for twist-bend modes are identical for suspensions with fast [1], slow or no concentration fluctuations.

Extensile Suspensions – For extensile systems, the most unstable modes are the pure bend modes with $\phi = 0$. In this case, (A3) and (A4) are identical and as discussed in the main text, a small q expansion reveals that the stability of the pure bend modes is governed by R . In Fig. 8(A,B) we plot the growth rate $\mathbb{I}(\omega)$ vs. q for pure bend modes at different values of R in regime A and B. The growth rate for a given $q \neq 0$ decreases with increasing R , and is order of magnitude smaller in regime B as compared to regime A.

The incompressibility constraint has major consequences on the stability of the $\phi \neq 0$ modes. The longitudinal and transverse fluctuations are coupled to each other and thus δp_x cannot be rendered *fast*, as was done previously in [1]. Further, incompressibility constraint eliminates the splay deformations by an equal and opposite contribution in the transverse direction which has a q -independent stabilizing effect. The relaxation rate does not vanish in the $q \rightarrow 0$ limit and at $q = 0$ we have one non vanishing eigenvalue $\omega_{\pm}^s = -2i\Gamma \sin^2 \phi$, which is a remnant of the coupling between δp_x and $\delta \mathbf{p}_{\perp}$. For small but nonzero ϕ , the splay contribution to these modes is small, and they are unstable in a manner similar to the pure bend modes but with a smaller growth rate and a smaller range of unstable wavenumbers. In Fig. 8(C) we plot $\mathbb{I}(\omega)$ vs. q for various values of ϕ at $R = 0.3$ and verify that indeed it is the case. The stability of the twist-bend modes is identical to that of the pure-bend modes, i.e., depending on the various values of R , we obtain three distinct regimes (See Fig. 1 in main text), but with a ϕ -dependent R_1 and R_2 . The dispersion relation for pure twist modes ($\phi = \pi/2$ in (A4)) reduces to $\omega_{\pm}^t = -\frac{i}{2\rho} (\mu_{\pm} \mp \mu_{\mp}) q^2$, implying that the pure twist modes are stable to linear perturbations.

Contractile Suspensions – Contractile suspensions go unstable via two dimensional splay perturbations and as a direct consequence of the incompressibility constraint on the order parameter, are always stable. This can also

be verified directly from (A3) and (A4). For example, the pure splay modes ($\phi = \pi/2$) relax with rates $\omega^s = \left(-i\frac{\mu}{\rho}q^2, -2i\Gamma\right)$, and twist-bend modes are always stable as $R < 0$.

-
- [1] R. Chatterjee, N. Rana, R. A. Simha, P. Perlekar, and S. Ramaswamy, *Phys. Rev. X* **11**, 031063 (2021).
- [2] R. A. Simha and S. Ramaswamy, *Phys. Rev. Lett.* **89**, 058101 (2002).
- [3] M. C. Marchetti, J. F. Joanny, S. Ramaswamy, T. B. Liverpool, J. Prost, M. Rao, and R. A. Simha, *Rev. Mod. Phys.* **85**, 1143 (2013).
- [4] S. Ramaswamy, *Annu. Rev. Condens. Matter Phys.* **1**, 323 (2010).
- [5] H. H. Wensink, J. Dunkel, S. Heidenreich, K. Drescher, R. E. Goldstein, H. Lowen, and J. M. Yeomans, *Proceedings of the National Academy of Sciences* **109**, 14308 (2012).
- [6] C. Dombrowski, L. Cisneros, S. Chatkaew, R. E. Goldstein, and J. O. Kessler, *Phys. Rev. Lett.* **93**, 098103 (2004).
- [7] L. Giomi, *Phys. Rev. X* **5**, 031003 (2015).
- [8] E. Lauga, *Annu. Rev. Fluid Mech.* **48**, 105 (2016).
- [9] E. Lauga and R. E. Goldstein, *Physics Today* **65**, 30 (2012).
- [10] E. Lauga and T. R. Powers, *Rep. Prog. Phys.* **72**, 096601 (2009).
- [11] R. Alert, J. Casademunt, and J.-F. Joanny, *Annu. Rev. Condens. Matter Phys.* **13**, 143 (2022).
- [12] L. Chen, C. F. Lee, and J. Toner, *Nat Commun* **7**, 12215 (2016).
- [13] M. E. Cates and E. Tjhung, *J. Fluid Mech.* **836**, P1 (2018).
- [14] P. Lenzi, *Cell Motility* (Springer Science+Business Media, LLC, New York, NY, 2008).
- [15] K. Kruse, J. F. Joanny, F. Jülicher, J. Prost, and K. Sekimoto, *Eur. Phys. J. E* **16**, 5 (2005).
- [16] P. G. de Gennes and J. Prost, *The Physics of Liquid Crystals*, 2nd ed., Oxford Science Publications No. 83 (Clarendon Press ; Oxford University Press, Oxford : New York, 1993).
- [17] S. Cox and P. Matthews, *Journal of Computational Physics* **176**, 430 (2002).
- [18] C. Canuto, M. Y. Hussaini, A. Quarteroni, and T. A. Zang, *Spectral Methods in Fluid Dynamics* (Springer Berlin Heidelberg, Berlin, Heidelberg, 1988).
- [19] In the limit $R \rightarrow 0$, we expect ξ (or d_{min}) to saturate to a value proportional to the core-radius of defects $\ell_c \equiv \sqrt{K}$ (independent of R).
- [20] S. Chandrasekhar, *Rev. Mod. Phys.* **15**, 1 (1943), Appendix VII.
- [21] P. Hertz, *Math. Ann* **67**, 387 (1909).
- [22] N. Rana and P. Perlekar, *Phys. Rev. E* **102**, 032617 (2020).
- [23] P. Grassberger and I. Procaccia, *Physica D: Nonlinear Phenomena* **9**, 189 (1983).
- [24] D. Mitra and P. Perlekar, *Phys. Rev. Fluids* **3**, 044303 (2018).
- [25] A. Wyner, J. Ziv, and A. Wyner, *IEEE Trans. Inf. Theory* **44**, 2045 (1998).
- [26] S. Martiniani, P. M. Chaikin, and D. Levine, *Phys. Rev. X* **9**, 011031 (2019).
- [27] S. Ro, B. Guo, A. Shih, T. V. Phan, R. H. Austin, D. Levine, P. M. Chaikin, and S. Martiniani, *Phys. Rev. Lett.* **129**, 220601 (2022).
- [28] $\theta(\mathbf{x}, t) = \tan^{-1}\left(\frac{p_y}{p_x}\right)$.
- [29] A. J. Bray, *Advances in Physics* **51**, 481 (2002).
- [30] U. Frisch and A. N. Kolmogorov, *Turbulence: The Legacy of A.N. Kolmogorov* (Cambridge University Press, Cambridge, [Eng.] ; New York, 1995).
- [31] S. Chandrasekhar, *Liquid Crystals*, 2nd ed. (Cambridge University Press, Cambridge [England] ; New York, NY, USA, 1992).